

Two-dimensional empirical rupture simulation: case study and applications to seismic hazard

Ethan Walsh¹, Tim Stahl¹, Andrew Howell^{1,2}, Tom Robinson¹

¹School of Earth and Environment, University of Canterbury, Christchurch, New Zealand

²GNS Science, Avalon, Lower Hutt, New Zealand

Abstract

Databases of historical surface rupturing earthquakes provide empirical constraints on the variables that influence multi-segment and multi-fault earthquakes. Here, we develop a numerical simulation that uses passing probabilities derived from surface rupture databases to characterize different rupture pathways initiating on a seed fault. The empirical rupture simulator (ERS) uses step distance, number of steps, angular change, and kinematic change to compute a combined passing probability for all fault section connections within 10 km of the seed fault and subsequent active ends of the propagating rupture. Ruptures end when all possible active ends fail to pass to the next section and the next iteration begins. We applied the ERS to two seed faults in the region of the 2016 Kaikoura (New Zealand) earthquake and compared the results to independent constraints on paleoseismic magnitude, segmentation, and global estimates of rupture complexity. Rupture set characteristics change dramatically based on seed fault location and indicate that kilometer-scale structural discontinuities serve as persistent barriers to rupture. Length-based magnitudes generally agree with those estimated from paleoseismic single event displacements. Our preferred model reproduces total trace complexity of historical earthquake catalogues and rarely generates 'Kaikoura-earthquake-type' events. Where appropriate, this semi-empirical approach may be useful for filtering or weighting on-fault maximum magnitudes in earthquake rupture forecasts. Alternatively, it could be used a straightforward tool for estimating maximum likely magnitudes. Further developments incorporating slip rate-based seeding might allow results to be compared to other established method of rupture simulation.

Introduction

Earthquake rupture forecasts are one major component of probabilistic seismic hazard analysis alongside ground motion models (e.g., Baker et al., 2021). In their simplest form, rupture sets underpinning such forecasts lead to annualized probabilities of rupture on independent seismic sources. Modern earthquake rupture forecasts account for scenarios in which multiple fault *sections* can rupture at once, including those that cascade across different fault segments and/or different faults (e.g. Field et al., 2014; 2017). Rupture sets are constructed so as to meet the slip rate requirements in inversions and often filtered to include only feasible ruptures that are computationally-tractable at later steps of analysis (Milner et al., 2013). To take an extreme example, it would be unhelpful to allow for simultaneous rupture of all faults in a nationwide database during a single rupture scenario, as this would (i) contradict observations of magnitudes and rupture complexity in historical earthquakes; (ii) undermine mechanical models of fault interaction; and (iii) introduce unnecessary (in terms of the inversion and output hazard) computational overhead in the form of many exceedingly unlikely ruptures. Thus, in both physics-based (Shaw et al., 2018) and probabilistic (e.g., Field et al., 2014; 2017) models, some assumptions are made to both allow for multi-fault earthquakes and constrain them to the most mechanically-feasible fault connections.

The third version of the Uniform California Earthquake Rupture Forecast (UCERF3) developed a set of plausibility filters to limit the number of ruptures included in the set (Milner et al., 2013). These criteria serve as Boolean filters to limit the number of ruptures to geologically-feasible and computationally-tractable scenarios. An additional approach detailed in Appendix J of the UCERF3 report (Biasi et al., 2013) proposed a set of empirically-derived *improbability constraints* that could be used to weight ruptures, based on the geometry and kinematics fault connections within them, compared against historical surface rupturing earthquakes. The same approach was proposed as a means to independently test outputs of the inversion process against the characteristics of historical surface rupturing earthquakes (Biasi et al., 2013).

Biasi and Wesnousky (2021) used two empirical variables affecting fault connection passing ratios to calculate conditional probabilities of rupture paths based on starting fault section. In their approach, penalties related to step size (km), and bend angle (degrees) derived from a compilation of mapped historical surface ruptures (Biasi and Wesnousky, 2016; 2017) are applied and compound serially with additional connections. The results are potentially valuable for Earthquake Early Warning (EEW) systems, as conditional probabilities for a range of ruptures can be pre-compiled for any starting fault section. That is, once an epicentral fault section is known, likely fault connections and rupture directions can be transmitted digitally to EEW systems more rapidly than seismic waves travel (Biasi and Wesnousky, 2021). Their work further demonstrates the potential utility of using empirical variables to forecast earthquake rupture pathways.

In this study, we developed an empirical rupture simulator (ERS) that generates different rupture pathways stemming from a starting (or 'seed') fault, similar to the approach of Biasi and Wesnousky (2021) (henceforth B&W2021). Our numerical

approach reads in pre-compiled, multi-variable co-rupture probabilities and performs a Monte Carlo simulation to test whether the ruptures propagate through fault connections at active ends of the rupture (Fig. 1). We apply this first version of the ERS to two seed faults in the New Zealand community fault model (Van Dissen et al., 2021; Seebeck et al., 2022) – the epicentral section of The Humps fault, which initiated the 2016 Kaikoura earthquake, and the western end of the Hope fault Conway segment – and compare the results to the numerical equivalent of B&W2021. The results of our preferred model produce magnitude distributions and overall complexity consistent with paleoseismology and global earthquake catalogues, respectively, and indicate significant differences in behaviour based on where ruptures initiate. The ruptures also qualitatively reproduce expected patterns of rupture arrest at segment boundaries and high-angle fault junctions. We discuss potential applications to seismic source characterisation and earthquake rupture forecasts more broadly.

ERS Assembly

Fault Co-Rupture Probabilities

The empirical variables used in this study were based on compiled databases of historical surface rupturing earthquakes in Wesnousky (2008), Wesnousky and Biasi (2011), Biasi and Wesnousky (2016), and Biasi and Wesnousky (2017). These compilations allow empirical passing ratios to be derived, which are defined as the proportion of ruptures passing a certain kind of fault connection to those arrested (Wesnousky and Biasi, 2011; Biasi and Wesnousky, 2016). Passing ratios can be translated into conditional co-rupture probabilities– for example, a passing ratio of 1 means that equal numbers of ruptures pass as are arrested for a given variable's value, which translates to a 0.5 co-rupture probability. Adequate data exist to directly derive co-rupture probabilities from passing ratios for *Step Size*, *Number of Steps*, and *Angular Change* variables (Table 1). B&W2021 use the product of *Step Distance* and *Angular Change* probabilities and interpolate the underpinning empirical data from previous studies only where data gaps exist. Accordingly, we used only *Step Distance* and *Angular Change* in our 'B&W2021 model' (Table 1).

In our other models, we used a mix of purely empirical and physics-based parameters based primarily on Biasi et al. (2013). The *Step Distance* variable (Table 1) penalizes steps between fault sections, such that small steps (or no step) have high passing probabilities which decrease with increasing step size. The equation that best fits historical surface rupture maps (Biasi and Wesnousky, 2016; B&W2021) is similar to two-dimensional physics-based models (e.g., Harris and Day, 1993; Shaw and Dieterich, 2007; Oglesby, 2008; and summarized in Biasi et al., 2013). We chose the exponential distance penalty of Shaw and Dieterich (2007) because it is a single, continuous function with probability of 1 at a step distance of 0, and improbable (but still possible) values for distances >5 km. We specified a hard threshold of 10 km above which ruptures could not jump to incorporate the full range of observations from the Kaikoura earthquake (Litchfield et al., 2018; Zinke et al., 2019; Nicol et al., 2022), and the need to constrain the number of possible fault connections computationally.

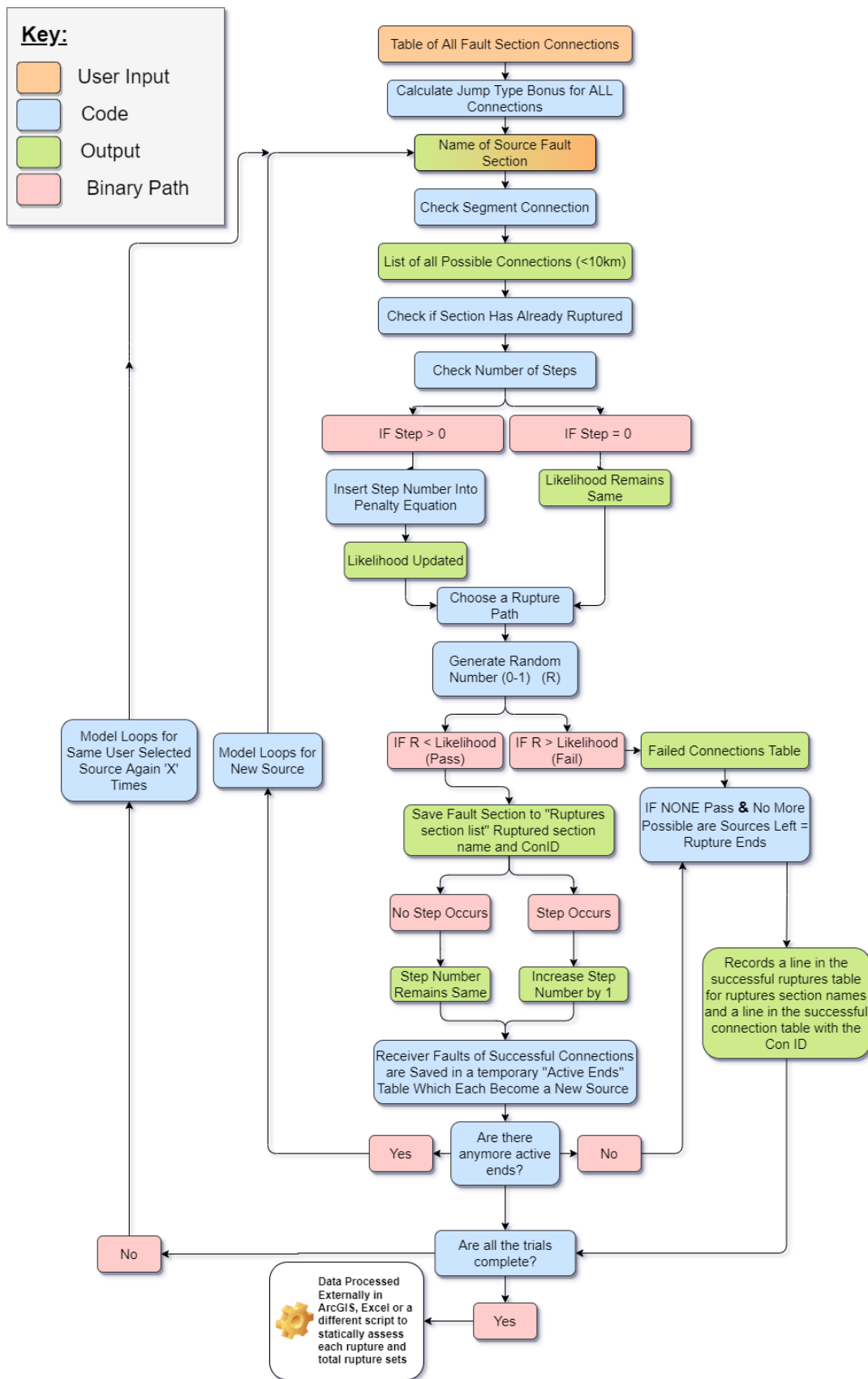


Figure 1: Simplified flow chart of the ERS algorithm. A more detailed version and description is found in the Supplementary Information. See text for discussion.

We used five variables in total in the ERS (Table 1). Four of the variables (step distance, number of steps, angular change, and kinematic change) act as penalties that serve to decrease the passing probability with decreasing co-rupture favorability (e.g. increasing step size or number of steps). These penalties were implemented because they have been demonstrated or inferred to dissipate the energy required for rupture propagation, even if, for example, the rupture is propagating from a source onto a high-angle conjugate receiver fault that is favourably oriented for co-rupture.

TABLE 1: Description of the variables used in the ERS.

Variable	Description	Type	Approach / Equation	References	Notes
<i>Step Distance</i>	The closest Euclidean distance between non-intersecting source and receiver fault section polygons	Penalty	For $x \leq 10$ km: $P(x) = e^{-x/r_0}$ where $r_0 = 1.44$ For $x > 10$ km: $f(x) = 0$	Shaw and Dieterich (2007); Biasi et al. (2013)	Limit of 10 km selected to allow unlikely but possible jumps.
			Curve fitting from B&W2021 Table 2: $P(x) = 1^{-0.2783x}$ Where x = step distance in km.	Biasi and Wesnousky (2016); Biasi and Wesnousky (2021)	
<i>Number of Steps</i>	Number of prior steps in rupture scenario	Penalty	$P_x(k) = pq^{k-1}$ where	Wesnousky and Biasi (2011); Biasi et al. (2013)	
<i>Stepover Type</i>	For strike-slip faults, bonus is applied to releasing steps	Bonus	Releasing steps: 1.4x passing ratio applied after calculating all penalties	Harris and Day (1993); Wesnousky (2006, 2008); Oglesby (2008)	Applied only when azimuth change is $\leq 30^\circ$, step distance is ≤ 5 km, and configuration and rakes are compatible with strike-slip
<i>Angular Change</i>	The change in azimuth from source to receiver fault sections	Penalty	Curve fitting from B&W2021 Table 2: $P(x) = 1^{-0.4129x}$ Where x = angular change ($< 180^\circ$) in degrees	Biasi and Wesnousky (2017); Biasi and Wesnousky (2021)	
<i>Kinematic Change</i>	The difference between source and receiver fault rake, from fuzzified categorical	Penalty	Categorical fault sense is translated to numerical values of rake change and passing ratio via fuzzy logic	Biasi et al. (2013)	See text and supplementary information for fuzzy logic detail

Step Distance and *Angular Change* are modelled as continuous variables as described above and in B&W2021. *Number of Steps* penalizes each successive step

(after the first) and incorporated as geometric distribution (after Wesnousky and Biasi, 2011; Biasi et al., 2013) (Table 1). *Kinematic Change* required conversion of categorical data regarding the slip sense of successful fault connections (Biasi et al., 2013) to source rake-receiver rake-passing probability space (Fig. 2). We used fuzzy logic for this conversion (details in the Supplementary Information). In general, certain connections like strike-slip to strike-slip were observed frequently in the historical record (Biasi et al, 2013), and are therefore considered favourable and assigned higher co-rupture probabilities than less likely (e.g. reverse-normal) connections. The process of converting categorical slip types to numerical rakes in this manner results in a maximum co-rupture probability of 0.92 between considered fault connections. This penalty has the affect of limiting rupture extent in the absence of any other penalties, for example, between sections on long, straight, and ‘mature’ strike-slip faults.

Stepover Type was implemented as a bonus and applied only to specific strike-slip fault connections. We chose to apply this variable as a bonus, rather than a penalty, to account for the slight favorability of releasing versus restraining steps (e.g. Harris and Day, 1993; Wesnousky, 2006; Oglesby, 2008; Li and Zhou, 2018), while avoiding over-penalizing steps. Final passing probabilities for all viable fault connections were calculated by multiplying those of individual variables in Table 1.

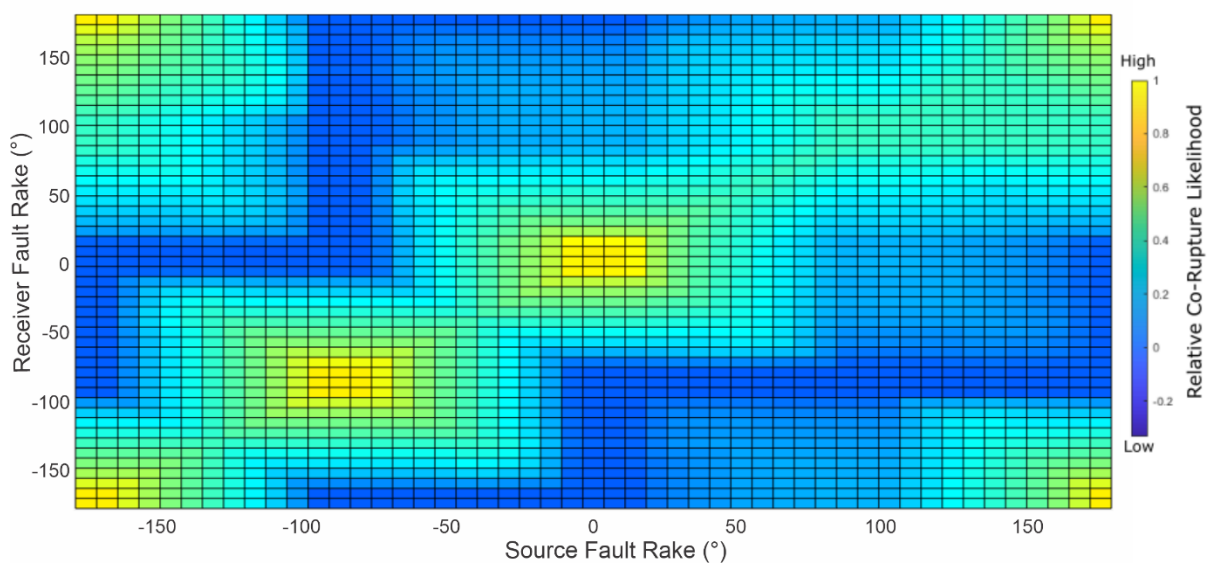


Figure 2: Overview of how kinematic change was tabulated at fault connections. The relative co-rupture likelihood (herein implemented as passing probabilities) are based on source fault section rake and receiver fault section rake. Co-rupture likelihoods are computed by taking the categorical weightings for fault-to-fault jumps in Biasi et al., (2013) and using fuzzy logic membership functions to assign rake. For example, a fault with a rake of 180° has a membership of 1 (full membership) to the strike-slip (dextral in this case) group, while a fault with a rake of 160° would have partial membership to both the strike-slip and reverse groups. Further details of this process are detailed in the Supplementary Information.

Pre-processing and overview of the algorithm

We used a modified version of the New Zealand Community Fault Model (Van Dissen et al., 2021; Seebeck et al., 2022) to identify and quantify the passing probabilities of all possible fault connections in the study area. Some simplification of fault traces was required to make them conform to the scale of the map compilations on which the empirical variables were based (i.e. minimum 5-7 km section length).

We trialled two levels of segmentation – one in which fault segments were between 5 and 10 km length, and the other in which there was no limit on maximum fault section length. In both cases, there is some user input into what constitutes a section boundary, which were usually defined by steps, bend, and or slip sense changes. To ensure *Angular Change* was $<180^\circ$, traces were re-drawn so that faults has consistent starting and ending directions. A fault trace buffer of 1 km (500 m either side of the fault and fault tips) was used to account for the simplification of traces and the potential for distributed faulting about the mapped trace. The distance between fault buffer polygons was used to discern what constituted a step and to calculate step distances. Intersecting polygons were considered to be contiguous faults. In practice, we found this buffer width ensured that small < 1 km steps at the surface were not considered as such, and counter-balanced the conservatism of the model in penalizing steps via multiple variables.

For a given seed fault, the ERS creates a rupture propagation path using empirically-informed passing ratios between fault sections. First, all connections from a fault section to surrounding fault sections within 10 km are considered (Fig. 1). For each connection, we simulate whether the rupture propagates between segments by conducting a random binomial (Bernoulli) trial, where the probability of success (rupture passing) is governed by the combined co-rupture probability between the two segments. If the rupture passes, then it continues onto this new section, and the process repeats until all possible connections are tested and have failed for that scenario (Fig. 1). If there are no more active sections, then the rupture scenario ends. The model then starts a new trial from the same original seed fault. This process is repeated 250,000 times to build each rupture set. The result is interpreted as being representative of the relative likelihoods of different unique rupture scenarios and classes thereof.

Test sites

We selected two seed faults for this test. The first seed fault is the epicentral section of the 2016 Kaikōura earthquake, located on The Humps fault (Nicol et al., 2018; Chamberlain et al., 2021). The unusual and complex rupture pattern of the Kaikōura earthquake (Hamling et al., 2017; Litchfield et al., 2018) was one of the motivations for creating ERS; one of the aims of using this seed fault was to test the hypothesis that the Kaikōura earthquake was the most complex on record, relative to other surface ruptures. As the specific configuration of faults that ruptured in the 2016 earthquake is exceedingly unlikely; we assess the model for ‘Kaikōura-type’ events, which include (i) rupture of The Humps fault and (ii) rupture of one or more faults in the Marlborough Fault System with order of magnitude higher slip rates (e.g. Litchfield et al., 2018). The rupture of one or more faults surrounding The Humps also contributes to matching the complexity of Kaikōura-type events, but has less of an effect on resultant magnitude comparisons.

The second seed fault is the westernmost section of the Hope fault’s Conway Segment (Figs. 3-8). The Hope fault was selected as its paleoseismology is relatively well constrained, and the slip rates make the fault one of the more prominent contributors to seismic hazard in the South Island (e.g. Stirling et al., 2012). The

Hope fault is considered the southernmost fault in the Marlborough Fault System, and is generally more ‘mature’ in its cumulative slip and long-term slip rate than faults to the south like The Humps. It is also bounded on its west by the pull-apart Hanmer Basin which is considered a major segment boundary and impediment to rupture propagation.

Overall, the two seed sections allow a comparison of different rupture set metrics against historical, paleoseismic, and structural constraints. The model domain (Figs. 3-8) was selected so as to allow ‘Kaikoura-type’ ruptures as well as full-length Hope fault ruptures.

Analysis

We considered three different model runs from each seed fault (Table 2), to compile a total of six rupture sets of 250,000 each. For each rupture set, we present (i) a frequency map, with each section coloured by the amount of times it ruptured out of 250,000; (ii) a moment magnitude (M_w) distribution, based on M_w -length scaling laws for surface rupturing strike-slip earthquakes in Wesnousky (2008); and (iii) a heat map of ranked relative likelihood versus M_w , with grid cells coloured by the number of unique rupture scenarios in given Rank – M_w bins (after Parsons et al., 2012). The frequency map in (i) shows the results of the entire 250,000 rupture set. In (ii) and (iii) we highlight excessively complex earthquakes based on the UCERF3 criterion *total absolute angular deflection (TAAD)*. TAAD is the cumulative angular change between adjacent sections within the rupture. UCERF3 used a value of 560° based on limits of historical surface ruptures, to allow ‘wall-to-wall’ ruptures of the San Andreas and to make rupture sets computationally tractable (Milner et al., 2013). For The Humps fault models, we highlight ‘Kaikoura-type’ ruptures in the text and maps of the maximum rupture length scenarios for each set are provided in the supplementary information.

Table 2: Model run properties. For each model (rows) ‘Y’ denotes ‘Yes’ for variables that were used and ‘N’ denotes ‘No’. Fault model segmentation characteristics are included under the title of each model (first column).

Model Run	Step Distance	# of Steps	Stepover Type	Angular Change	Kinematic Change
<i>Unsegmented</i> (minimum 5 km section length; no maximum)	Y	Y	Y	Y	Y- all section boundaries
<i>B&W2021</i> (5-10 km section lengths)	Y	N	N	Y	N
<i>Segmented</i> (5-10 km section lengths)	Y	Y	Y	Y	Y- steps only

Known assumptions and limitations

It is important to stress the overarching assumptions and limitations in tabulating passing probabilities and assembling rupture sets using this approach.

- 1) Scale and Mapping Quality in Underpinning Data:** The quality of surface rupture mapping is a fundamental component of developing empirical 'rules'. Not all ruptures are mapped in the same level of detail and the record of all past ruptures is incomplete. However, the minimum section length of 5-7 km used by Wesnousky (2008) and Biasi and Wesnousky (2016, 2017) when mapping historical ruptures reduces the uncertainty and need for detailed mapping at <1 km resolution. However, there are still arbitrary calls made by the user when defining and simplifying fault sections, which ultimately affect the calculation of passing probabilities.
- 2) Two dimensions:** The empirical relationships used in the ERS are derived only for surface ruptures in map view because 3D data is usually unavailable. While many historical events will include faults with interactions at depth, there is an inherent lack of resolution in applying 2D rules to 3D problems. This problem is especially pertinent for ruptures involving or connecting through faults or regional detachments that are unmappable or do not reach the surface, which may be the case for the Kaikoura earthquake (e.g., Hamling et al., 2017; Litchfield et al., 2018). If this is the case, then we would expect Kaikoura-type events to be impossible or exceedingly rare, relative to other events starting on The Humps fault.
- 3) Bias in underpinning data and issues applying them to other faults:** Historical ruptures in the Biasi and Wesnousky (2016, 2017) datasets and others used to derive the empirical rules herein are from predominantly strike-slip ruptures. The relative lack of data on dip-slip ruptures means that the ERS is biased towards strike-slip dominated tectonic settings. While in some cases reasonable relationships can be drawn for dip slip faults as well (e.g. for angular change), the 'robustness' may be diminished due to having fewer data. Additionally, in the northern South Island of New Zealand, many faults have oblique sense of slip, so determining which relationship to use becomes a judgement call. We used all strike-slip-related rules for consistency and the fact that it is the primary mode of slip in the model domain.
- 4) Variable conservatism:** Some connections that are kinematically favorable, such as conjugate faults, are often heavily penalised in the ERS through both kinematic and azimuth change parameters. While these rupture propagating onto these connections may still dissipate seismic energy and reduce the likelihood of co-rupture relative to straight ruptures with the same sense, the ERS may overly- penalize these geologically favorable connections. The B&W2021 model we present is the most liberal in this regard, as it does not include kinematic change. This reinforces the fact that the main aim of the ERS is to compare the relative likelihoods of rupture scenarios (e.g. Parsons et al., 2012) rather than accurately assess absolute likelihoods.
- 5) Model conservatism and non-independent variables:** The penalties were derived and applied independently, but there may be some interdependencies of parameters. This could serve to over-penalise some connections, which would make the ERS co-rupture probabilities conservative compared to other

methods. For instance, our models penalize steps twice. We ultimately used *Number of Steps* in addition to *Step Distance* on the basis that each successive step compounds the energy lost by rupture irrespective of distance (e.g. Oglesby 2008; Wesnousky and Biasi, 2011).

Overall, we believe that by presenting three models spanning the spectrum from 'conservative' to 'liberal' parameters, we present severable viable options for researchers wanting to use a similar approach.

Overview of Model Results

Seed fault sections rupture in every iteration by definition. As expected based on pre-assembled probabilities, the seed fault and ≥ 1 adjacent sections rupture in the same scenario very frequently ($>40\%$ of ruptures in all but one rupture set) (Figs. 3-8A). Longer single-fault and multi-fault earthquakes occur with varying rupture frequencies depending on the model parameters (Table 2), but section rupture frequency generally decreases with increasing length and/or rupture complexity (Fig. Figs. 3-8A). Magnitude distributions (Figs. 3-8C) reflect preference for multi-section earthquakes in all but one rupture set (Fig. 3B), in which the majority of ruptures arrested on the seed fault. Individual modes in the M_w distributions are sometimes associated with classes of ruptures. For example, in the Hope fault simulations (Figs. 6-8), there is a preference for full-length or near-full-length ruptures of the Conway Segment of the Hope fault, resulting in a mode near M_w 7-7.3. In the B&W2021 model for The Humps fault, three modes can be detected, that loosely correspond to Humps fault, Humps-Hope fault, and Humps-Hope-Alpine fault rupture classes (Fig. 4C). Rupture sets have somewhat erratic magnitudes at the scale of 1-2 fault section lengths, which depends on section length (based on model segmentation; Table 2) and fault complexity adjacent the seed fault. UCERF3 defines a rupture as including 2 or more sections, but we chose to leave single section ruptures in the sets to highlight the effects of different model parameters.

We note here that most of the M_w distributions follow truncated- or concatenated normal distributions (Figs. 3-8C) and therefore do not conform to a Gutenberg-Richter (G-R) relationship. This was expected, given the non-random seeding of faults in the model and construction of the model inputs based solely on $c. >M_w$ 6 surface rupturing earthquakes. However, heat maps of ranked relative likelihood (Figs. 3-8B) show a steep drop-off in the frequency of events and ranked likelihood at higher magnitudes. The captions for Figures 3-8 discuss the implications of individual heat maps in more detail; however, this drop-off could demonstrate a potential use of our method in seismic hazard studies as a way of determining the maximum likely magnitude of earthquakes for a given source or region.

Differences Between Models

The differences between our models are dictated by the number of penalties being imposed, the number of fault sections (i.e. segmentation), and how kinematic change penalties get applied (Table 2). Because of its fewer penalties, B&W2021 rupture sets are the most 'liberal' and produce longer, more complex rupture sets than the other two. In the Unsegmented model, there is a tradeoff between maximum section length, which is unconstrained and therefore 'liberating', and kinematic change,

which is calculated at every fault section connection, and therefore 'conserving' relative to the Segmented model. Our results indicate that the effect of calculating kinematic change at every section boundary makes the Unsegmented model more conservative in that it results in shorter, less complex events than those in the Segmented model.

While further development would be required to cross-validate the various model results with e.g. physics-based simulation (namely, accounting for slip rate and not specifying seed faults), we prefer our Segmented model over the Unsegmented model based on how kinematic change is implemented. Whereas the Segmented model penalizes rake change at every section boundary, even those along contiguous sections of straight faults, the Unsegmented model only penalizes changes where steps are detected (i.e. adjacent fault zone polygons do not intersect) (Table 2). This restriction was imposed because the categorical weightings in Biasi et al (2013) were tabulated specifically for fault-to-fault jumps, not for individual sections within contiguous ruptures. Additionally, because of the process used to convert categorical kinematic data to numerical rakes, the smallest penalty that adjacent sections can incur due to kinematic change in the Unsegmented model is 0.92 (Figure 2; Supplementary Information). That is, even when fault sections do not change rake, the highest probability of passing is 0.92, regardless of other factors. This bound on the kinematic change penalty was preferable for limiting automatic wall-to-wall ruptures on straight contiguous fault sections (e.g. Biasi and Wesnousky, 2021) but may over-penalize otherwise favourable connections.

We also prefer the Segmented model because it results in rare, large events similar to the Kaikoura earthquake for events originating on The Humps fault (upper magnitude bound of M_w 7.9; Fig. 5C). The Unsegmented model for The Humps fault maxes out at M_w 7.2 (Fig. 3C) and never leads to rupture of the Kekerengu or Alpine faults (Fig. 3A). While these are undoubtedly rare events (Litchfield et al., 2018; Hatem et al., 2019; and discussed more below), we maintain that they should be in the realm of possible outcomes based on the Kaikoura earthquake and preliminary physics-based simulation results (Shaw et al., 2022). In subsequent discussion we therefore focus on the results of our preferred model and those of the B&W2021 model against 'reality checks' that serve as first-order measures of model performance.

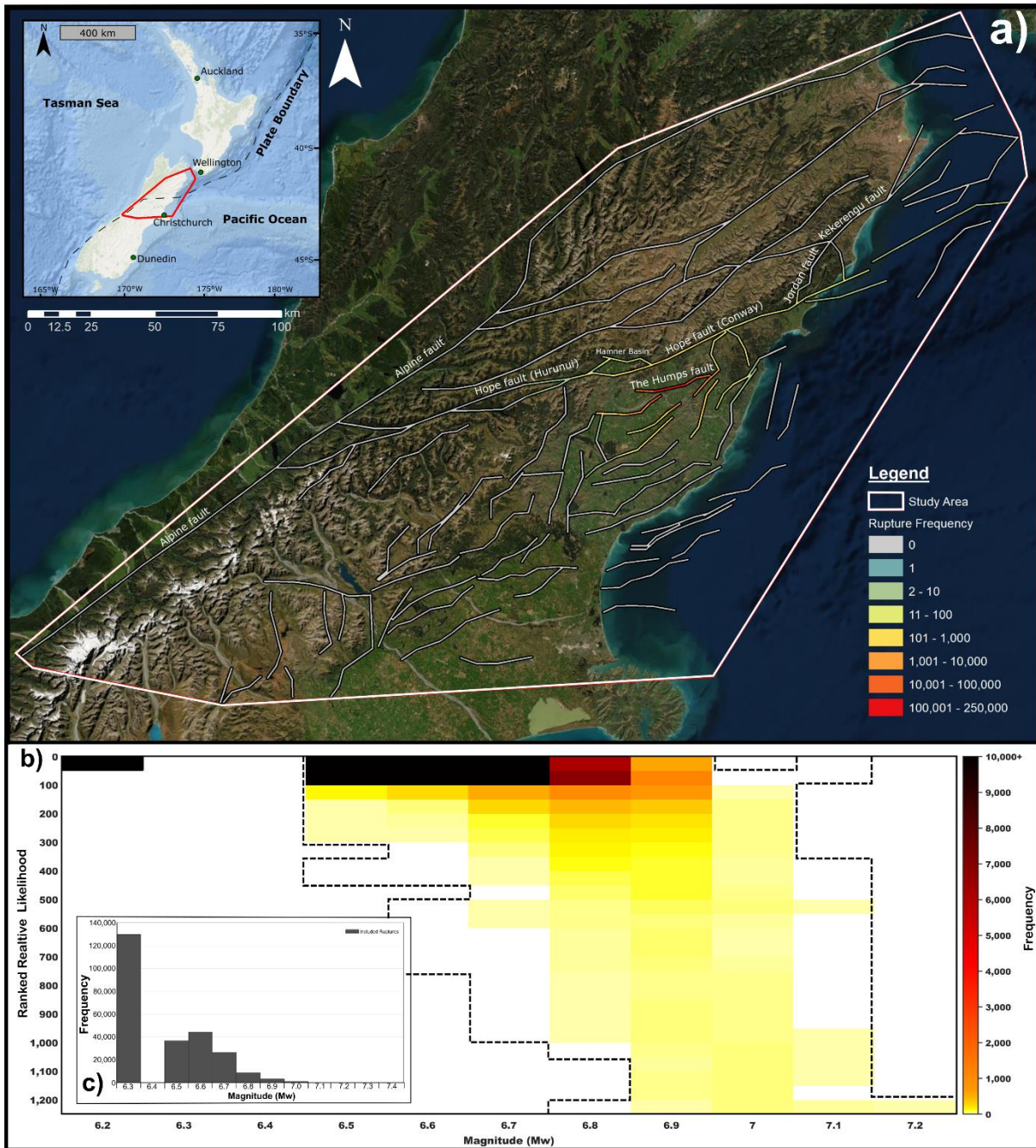


Figure 3: Unsegmented model results for The Humps fault. For all Figures 3-8, the red bounding polygon in the inset shows the location of the study area in the NE South Island, New Zealand. The same bounding box is shown in (a) for reference. In (a), individual fault sections within the New Zealand Community Fault Model are colored by number of times ruptured. Fault sections that did not rupture in any of the 250,000 trials are shown in light gray. The major fault names and segments discussed in text are labelled. In (b), the magnitudes, frequency, and ranked relative likelihood of unique scenarios are plotted. Each rupture scenario is assigned a ranked relative likelihood based on the number of times those specific combinations of fault sections appear in the rupture set. Moment magnitude (M_w) is plotted on the x-axis. Grid cells of rank \times magnitude vary based on model run; in this figure they are 50×0.1 , respectively. Grid cells are colored by the frequency of ruptures occupying that grid space. Dashed lines are the boundaries of the full dataset, as ruptures that appear ~ 1 time are not colored. Heat maps are useful for identifying relative likelihoods and magnitudes of classes of unique ruptures. In this instance, there are only ~ 200 unique configurations that produce M_w 6.3-6.8 events, but these recur very frequently (red shading). There are several hundred unique configurations that produce $\geq M_w$ 6.9 events, but recurrence of those events is very uncommon (yellow shading). A simple histogram of magnitudes is shown in (c). Note that in both (b) and (c), there is a gap at M_w 6.4 as no combination of section lengths could result in that particular magnitude for an event originating on the central Humps fault. Ruptures in this model tend to stay on The Humps fault and only rarely propagate beyond adjacent sections. None of the events reach the Kekerengu fault. No events were exceeded our TAAD threshold of 560° ; in subsequent figures, (a) and (b) include the entire unfiltered rupture set, whereas (c) does not.

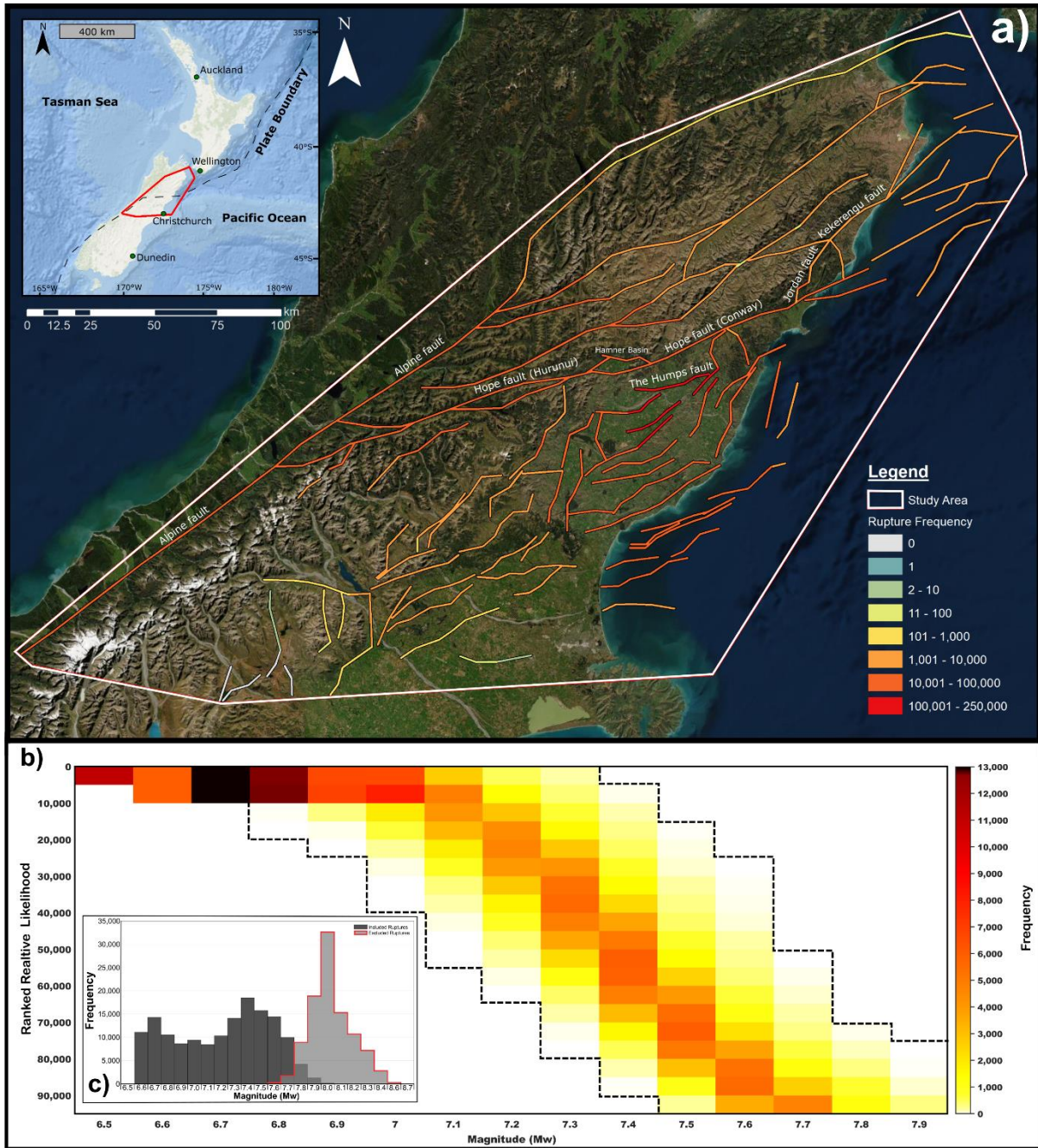


Figure 4: B&W2021 model results for The Humps fault. See Figure 3 for a description of all figure elements; grid cell size in (b) is 5,000 x 0.1 due to a significantly larger (~x100) number of unique ruptures. The frequency of multi-fault earthquakes in the model is relatively high compared to the Unsegmented model. More ruptures than not extend beyond sections of The Humps fault, although the most frequent unique configuration is that of a Humps fault rupture (dark red shading in (b)). The descending diagonal zone of red shading in (c) highlights that there are tens of thousands of unique configurations faults that as a class of multi-fault earthquakes occur very frequently. Over 1,000 ruptures reach the Kekerengu fault and over 10,000 reach the Alpine fault, but many of these exceed the TAAD complexity threshold as shown in red-outlined histogram in (c). 98,579 ruptures were filtered based on TAAD.

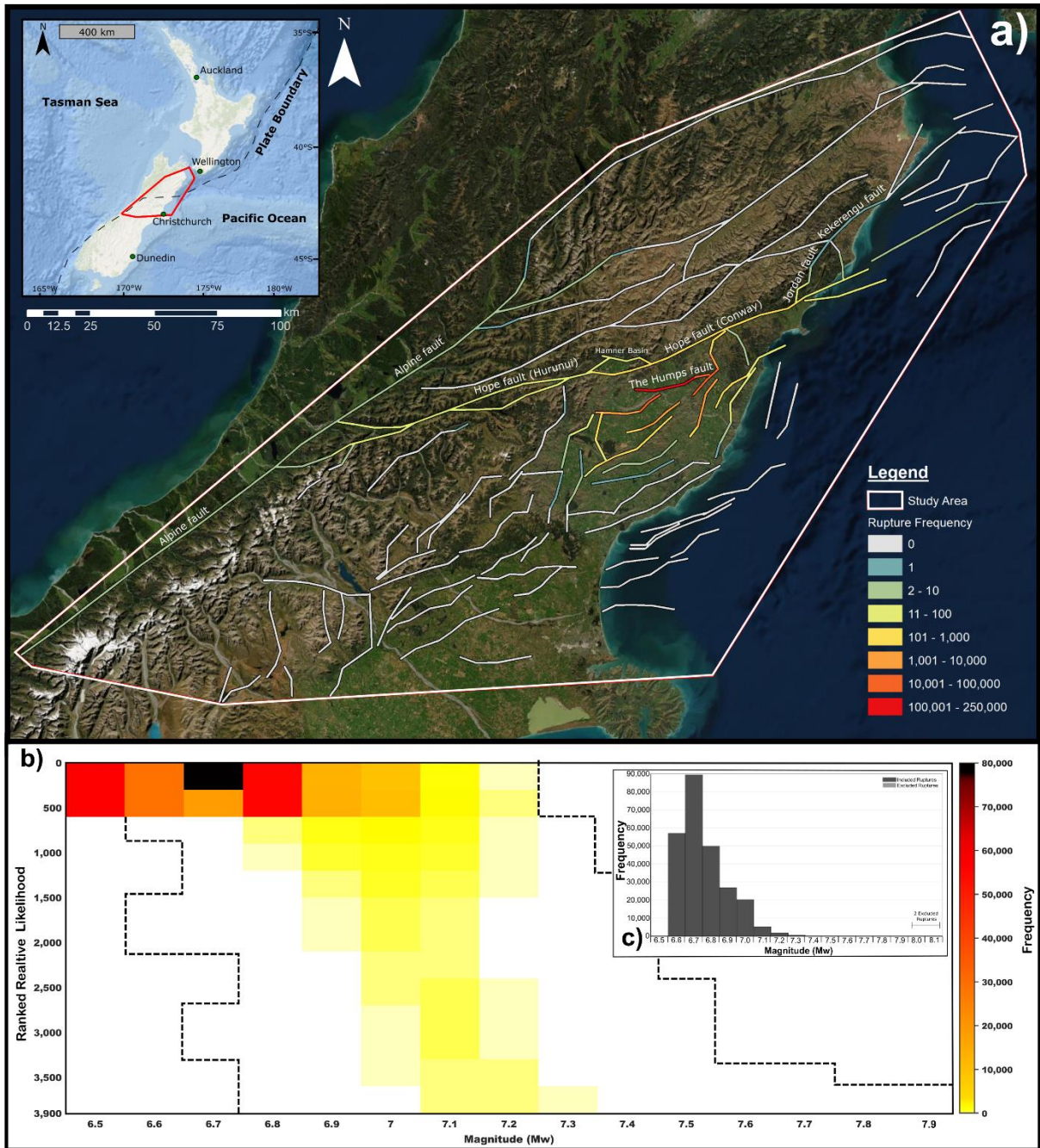


Figure 5: Segmented model results for The Humps fault. See Figure 3 for a description of all figure elements; grid cell size in (b) is 300×0.1 . In (c), ~ 500 unique configurations account for the vast majority of ruptures, with most of these being $M_w 6.7$ Humps fault events. While most events stay on The Humps fault, there is a large class of ruptures (yellow shading and dashed lines in (b)) that extend further, with some constituting $M_w 7.9$ events. One rupture reached the Kekerengu fault and seven reached the Alpine fault via the Hope fault in (a). Two ruptures were filtered based on TAAD as demarcated in (c).

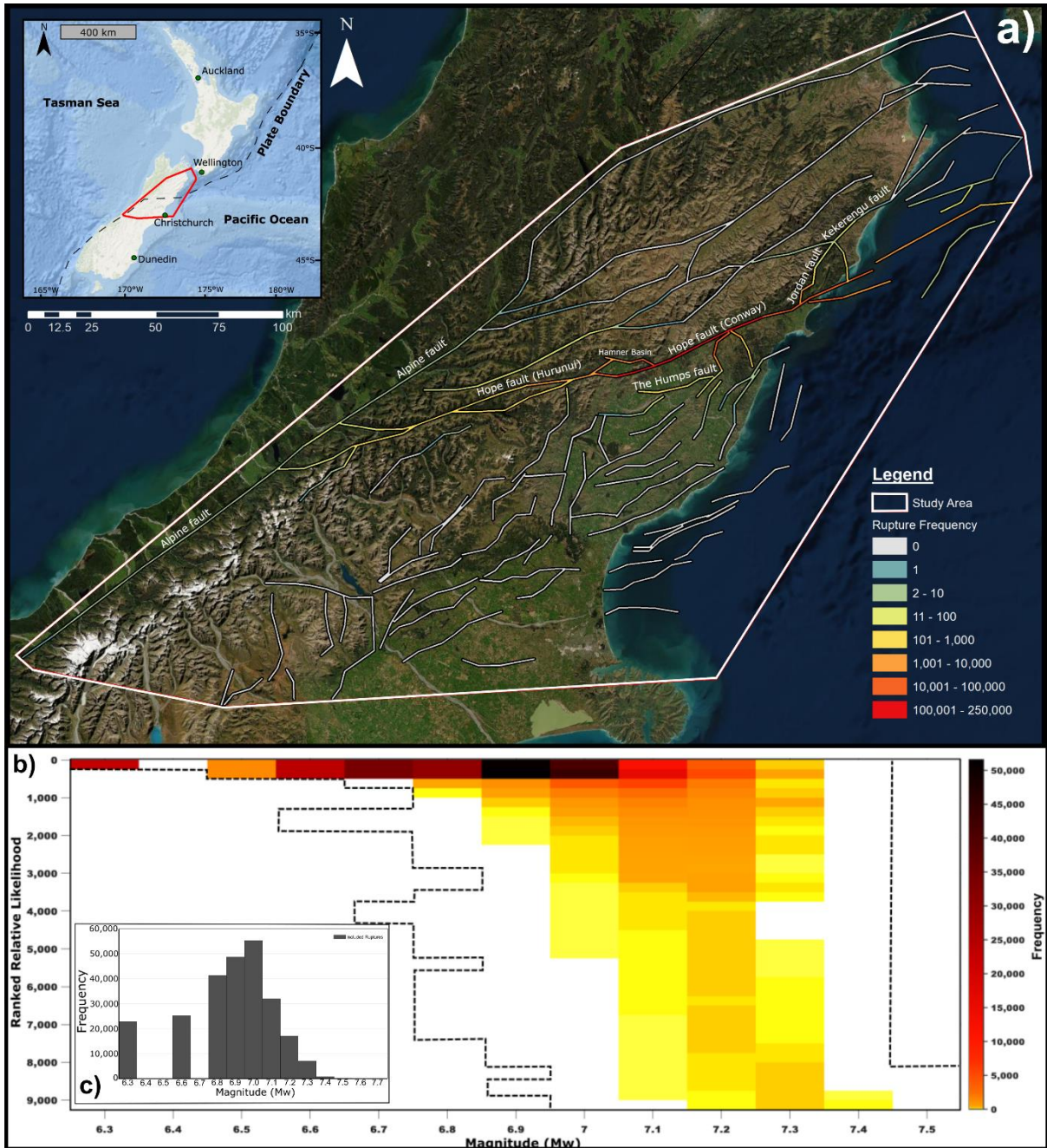


Figure 6: Unsegmented model results for the western Conway Segment of the Hope fault. See Figure 3 for a description of all figure elements; grid cell size in (b) is 250×0.1 . Ruptures preferentially propagate to the NE along the Conway Segment ($>10^5$ events) in (a); comparatively fewer ruptures propagate W across the Hamner Basin pull-apart and onto the Hurunui Segment (10^2 - 10^4 events). Connections to other faults in the Marlborough Fault System and North Canterbury are possible, as is connection to the Alpine fault in the west, though sharp angle changes at these connections makes them unlikely. The most common class of ruptures comprises near-full-length ruptures of the Conway Segment. No events were filtered based on TAAD.

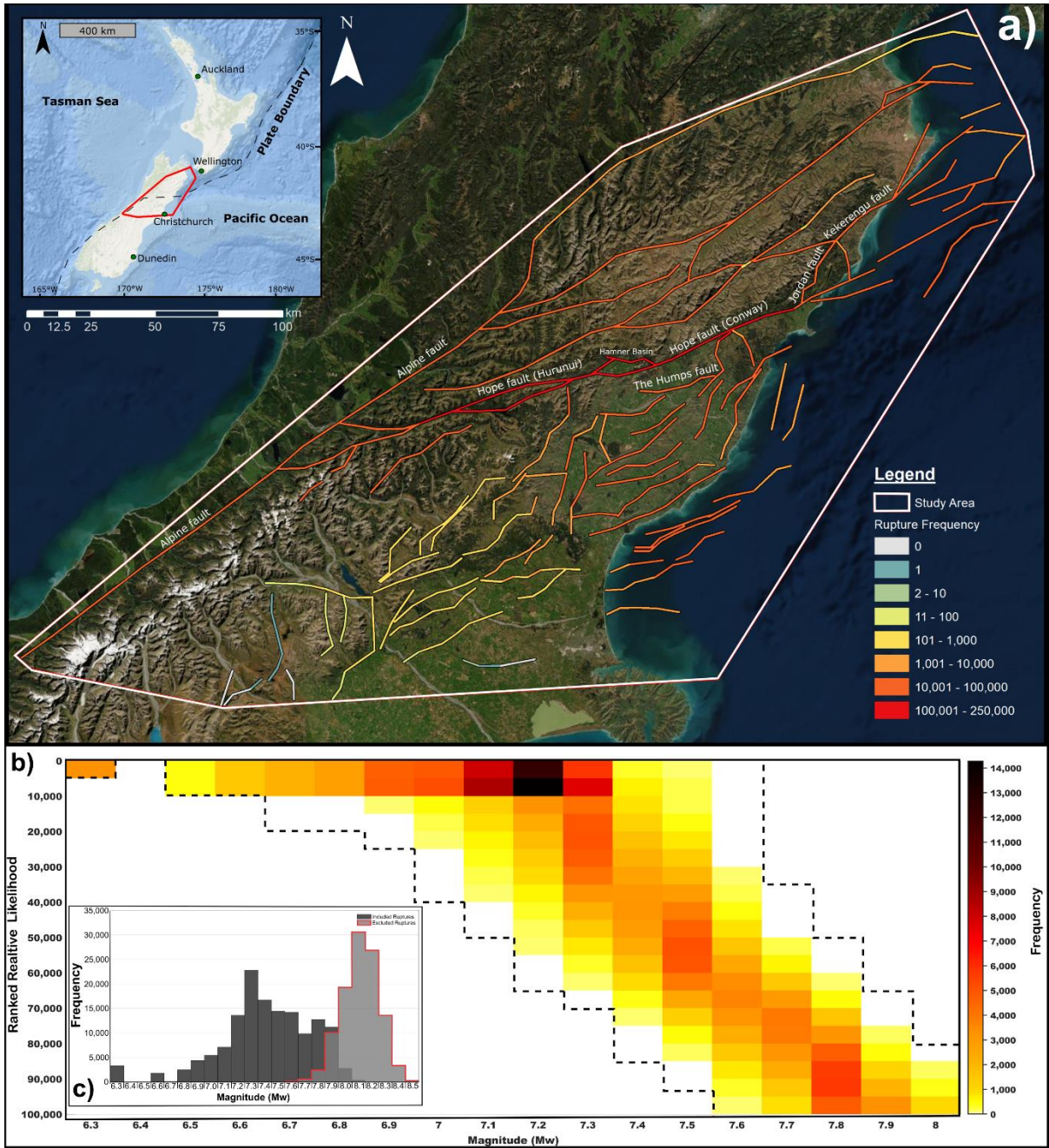


Figure 7: B&W2021 model results for the Hope fault. See Figure 3 for a description of all figure elements; grid cell size in (b) is $5,000 \times 0.1$. Similar to the B&W2021 model for The Humps fault, there is a propensity for multi-fault events, and many unique configurations of them, though the most common class of ruptures comprises Conway to Hurunui segment ruptures of the Hope fault. 106,774 ruptures were filtered based on TAAD (shown in (c)).

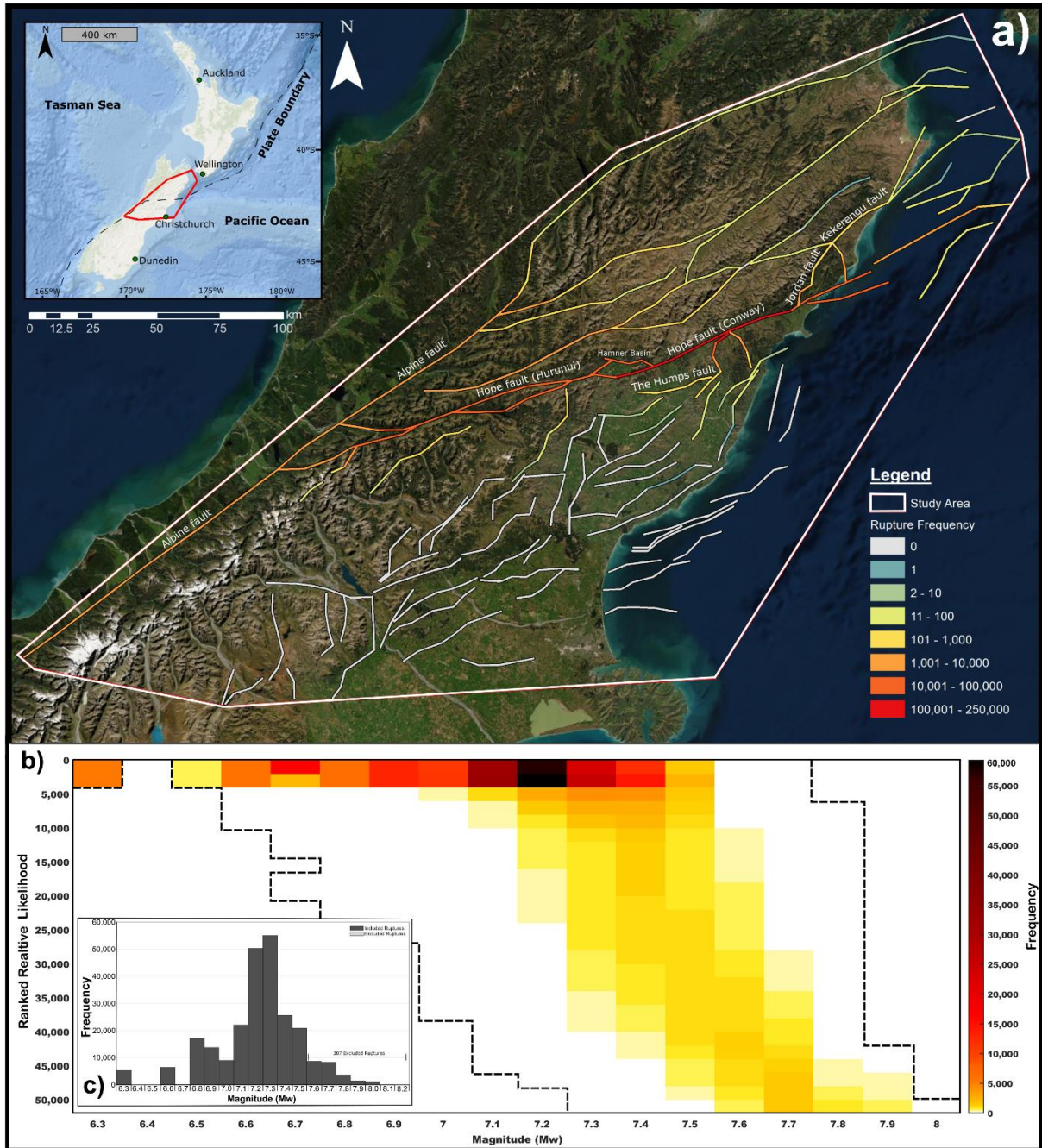


Figure 8: Segmented model results for the Hope fault. See Figure 3 for a description of all figure elements; grid cell size in (b) is 2,000 x 0.1. The most common class of ruptures comprises full-length ruptures of the Conway Segment, with comparatively fewer ruptures propagating past the Hammer Basin pull-apart to the Hurunui Segment and past intersection with the Jordan fault. Despite this pattern, there are many possible unique configurations of multi-fault or multi-segment earthquakes, as shown by the descending diagonal of orange shaded cells in (b). 307 ruptures were filtered based on TAAD.

Reality Checks on Preferred Model

Do ruptures conform to historical measures of rupture complexity?

The complexity of modelled ruptures relative to historical earthquakes may be an indicator of model performance. We plotted the TAAD versus Rupture Length and TAAD/km (or curvature) versus Rupture Length for historical earthquakes (Biasi and Wesnousky, 2017) and the model runs for each seed fault separately (Fig. 9). In each, the TAAD filter of 560° is plotted along with the ruptures that were excluded from analysis in Figures 3-8B. The extent of historical earthquakes corresponds most closely to that of our Segmented model, particularly when curvature (TAAD/km) is considered (Figs. 9C and D). Although angular change is penalised in all of the models, the output TAAD is simply calculated after the rupture ceases and is an emergent property of the data. All three of our models are capable of reproducing the complexity of the northern Kaikoura ruptures (i.e. faulting north of the Hope fault, Figs.3-8) but very few scenarios or historical earthquakes match the complexity of the southern ruptures (Fig. 9).

The extent of the Segmented model also conforms most closely to the UCERF3 TAAD filter threshold, and while this observation alone does not necessarily indicate that it is a more realistic rupture set, it does highlight that excessively long (e.g. >500 km) and/or complex (e.g. fully-circular) ruptures do not tend to occur in this model. The B&W2021 model does produce significant numbers of ruptures beyond the bounds of historical earthquakes and outside the UCERF3 complexity threshold. We infer that in the tectonic setting of the NE South Island, comprising closely-spaced faults within a zone of distributed oblique transpression, the parameters in the Segmented model lead to more realistic results.

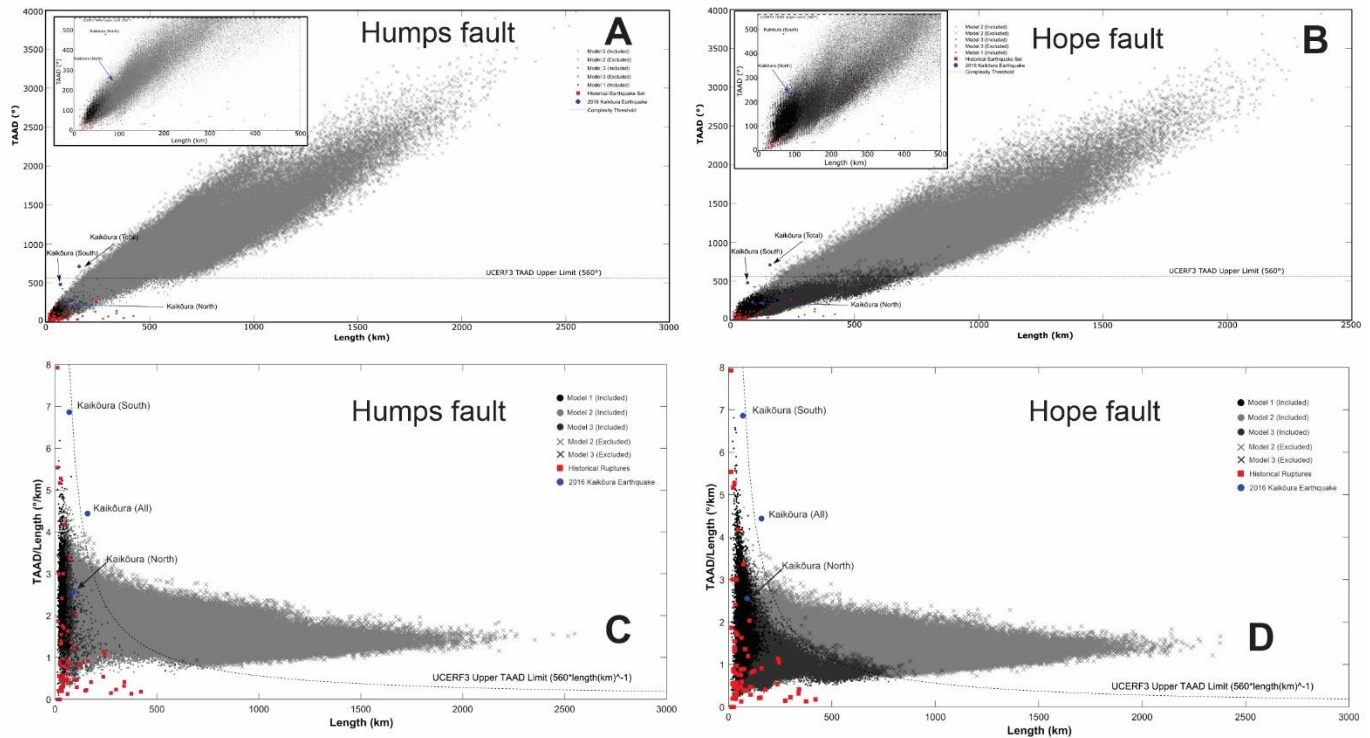


Figure 9: Rupture complexity as measured by total absolute angular deflection, or TAAD (A and B) and curvature, or TAAD/km (C and D). In each figure, red squares represent historical earthquake surface ruptures, gray represent our three model runs, and blue circles are measured from the Kaikōura earthquake. Our segmented model (Model 3, medium gray) share the most overlap with historical earthquake ruptures and generally fall within the UCERF3 TAAD threshold of 560°. Density plots for these data can be found in the Supplementary Information.

Do segment boundaries and structural barriers tend to impede rupture propagation?

The frequency with which known or expected barriers are breached might be an indicator of model performance. The most well-known barriers to rupture propagation in the model area are the Hanmer Basin pull-apart basin, which demarcates the boundary between the Conway and Hope River Segments of the Hope fault, and the eastern end of the Conway Segment, where the majority of long-term strain is transferred onto the Kekerengu fault to the north through the Jordan fault (Little et al., 2018; Howell et al., 2019).

Historical events and paleoseismology suggest that most ruptures along the Hope fault are bound to geologically-defined segments (Cowan and McGlone, 1991; Langridge et al., 2003; Khajavi et al., 2016). The 1888 Amuri earthquake was predominantly bound to the Hope River segment of the Hope fault (Cowan and McGlone, 1991; Khajavi et al., 2016) and it is generally accepted that the rupture did not propagate through the Hanmer basin (Cowan, 1991; Langridge and Berryman, 2005; Khajavi et al., 2016).

The timing and recurrence intervals of earthquakes vary along the length of the Hope fault and loosely constrain segmentation. The Conway segment of the Hope fault has evidence of rupturing five times in the last ~2000 years (Khajavi et al., 2016; Hatem et al., 2019). The Hope River segment of the Hope fault only has two recorded surface rupturing events: the 1888 Amuri earthquakes and a second between 1118–1609 (Cowan and McGlone, 1991; Langridge et al., 2013; Khajavi et

al., 2016). Hatem et al. (2019) argue that paleoseismic evidence indicates the possibility of rare full-length ruptures occurring along the Hope fault, but that it would have to be uncommon (at least within the last ~2,000 years). This interpretation is also consistent with reduced fault slip rates beyond the eastern end of the Conway Segment near its intersection with the Jordan fault and Seward Segment.

Our preferred model indicates that the Hanmer Basin and intersection with the Jordan fault-Seaward Segment act as persistent but penetrable barriers to rupture propagation (Fig. 8A). Approximately 13% of ruptures (~32.5k) propagate through the entire Hanmer Basin, meaning that it arrests rupture ~87% of the time. This is slightly lower than the ~95% estimate of Robinson (2004) synthetic seismicity model based on Coulomb stress triggering. Approximately 15% of ruptures (51k) propagate to the Jordan fault from the Conway Segment with 85% being arrested. This estimate is consistent with the 86% arrested (or not triggered) in Robinson (2004).

Do independent magnitude estimates coincide with modal magnitudes?

Both The Humps and Hope faults have been the subjects of paleoseismic and geomorphic investigations from which displacement-based magnitude estimates can be derived. While many of these magnitude estimates come from single sites along the faults, and therefore may not be representative of either mean or maximum displacement used to calculate magnitude from empirical scaling laws, these magnitudes provide first-order, independent estimates for comparison to our rupture length-based models.

The most common scenario in our preferred model is M_w 6.7 near-full-length ruptures of The Humps fault. Full length Humps fault earthquakes in our fault model are 30.1 km and correspond to a ~ M_w 6.84 event. One paleoseismic site on The Humps fault documented vertical displacements associated with past surface rupturing earthquakes (Brough et al., 2021). Assuming a horizontal:vertical slip ratio as that of the Kaikoura earthquake, the net slip in the past two events would be 1.1 and 2.8 m, which roughly coincide with the average and maximum net displacements in 2016 (Nicol et al., 2018). If these are accepted as average displacements for The Humps fault, they would correspond to ~ M_w 7.0-7.3 events; if they are accepted as maximum displacements they would correspond to M_w 6.7-7.0 events (using scaling of Wells and Coppersmith, 1994). While significant uncertainties exist in making this comparison, the magnitude distribution for our preferred model (Fig. 5C) is generally in line with magnitudes estimated from paleo-earthquake displacements.

The most common scenario in our preferred model of the Hope fault is M_w 7.2-7.3 full length ruptures of the Conway Segment (Fig. 8C). Beauprêtre et al. (2012) used ground-penetrating radar and lidar to investigate the rupture history and single event displacements along the Conway segment. The authors inferred that there had been ~10 surface ruptures along the Conway segment with an average coseismic slip of 3.3 ± 1 m corresponding to M_w 7.0-7.4 events. Thus, there is decent agreement between the two independent estimates of magnitudes. By comparison, the B&W2021 model results in a mode around M_w 7.3-7.4, but with secondary modes at ~ M_w 7.8 and ~ M_w 8.1 in the filtered and unfiltered data, respectively. These modes reflect the higher number of ruptures that cascade onto other faults and fault

segments. These events are not necessarily unrealistic on their own, but are more difficult to reconcile with previously reported single event displacements for the Conway Segment.

How likely was the Kaikoura earthquake?

The ability to reproduce Kaikoura-type events for rupture originating on The Humps fault might be an indicator of model performance. Of course, the specific configuration of surface ruptures in the 2016 Kaikoura earthquake is unlikely considering the full range of possible rupture pathways. We would also expect Kaikoura-type events to be relatively rare, considering the order of magnitude range of slip rates for the faults that did rupture (e.g. Litchfield et al., 2018). In the preferred (Segmented model), the Kekerengu fault ruptured in a single scenario (Fig. 10). There are 253 ruptures (~0.1%) that include five or more sections of the Hope fault. There are another ~250 ruptures that include the full Humps, Leader and partial Hundalee faults (and occasional other sections of adjacent faults). This places the approximate relative likelihood of a Southern 2016 Kaikōura type rupture at ~0.1%.

Although the absolute likelihood of Kaikoura-type events is unclear, they are evidently unlikely relative to other events in our ruptures sets (e.g. Fig. 5B). While it is possible that Kaikoura-type events are truly rare (<1% of ruptures starting The Humps fault), other possible explanations include unmodelled subsurface fault connections (Litchfield et al., 2018) and/or unmodelled offshore faults (e.g. Nicol et al., 2022). It is also possible that the complexity of the Kaikoura earthquake (Fig. 9) is in part due to counting secondary surface ruptures in the Southern region as primary surface rupture. Overall complexity is reduced if one or more of these faults failed due to e.g. large scale block rotations driven by other faults, which would make the Kaikoura earthquake less of an outlier compared to historical data and model results (Fig. 9)

Potential Use in Seismic Hazard

Pre-compiled fault connection probabilities have potential uses in EEW (Biasi and Wesnousky, 2021). They may also be used to weight specific rupture scenarios compiled using other methods (Biasi et al., 2013; Field et al., 2014). The results of numerical simulations like ours might also be useful in characterizing the maximum likely magnitudes for epicentral fault sections (Figs. 3-8C) or for an entire region, if all possible epicentral sections are considered. This simple semi-empirical approach could be developed to incorporate known fault slip rates, making the resulting rupture sets more comparable to e.g. physics-based simulations. Such an approach could, for example, pseudo-randomly seed ruptures based on geologic slip rate. While further work is required to ensure the model provides reasonable results, slip rate-based seeding might be one method of cross-validating first order results like maximum magnitudes and frequency of multi-fault earthquakes.

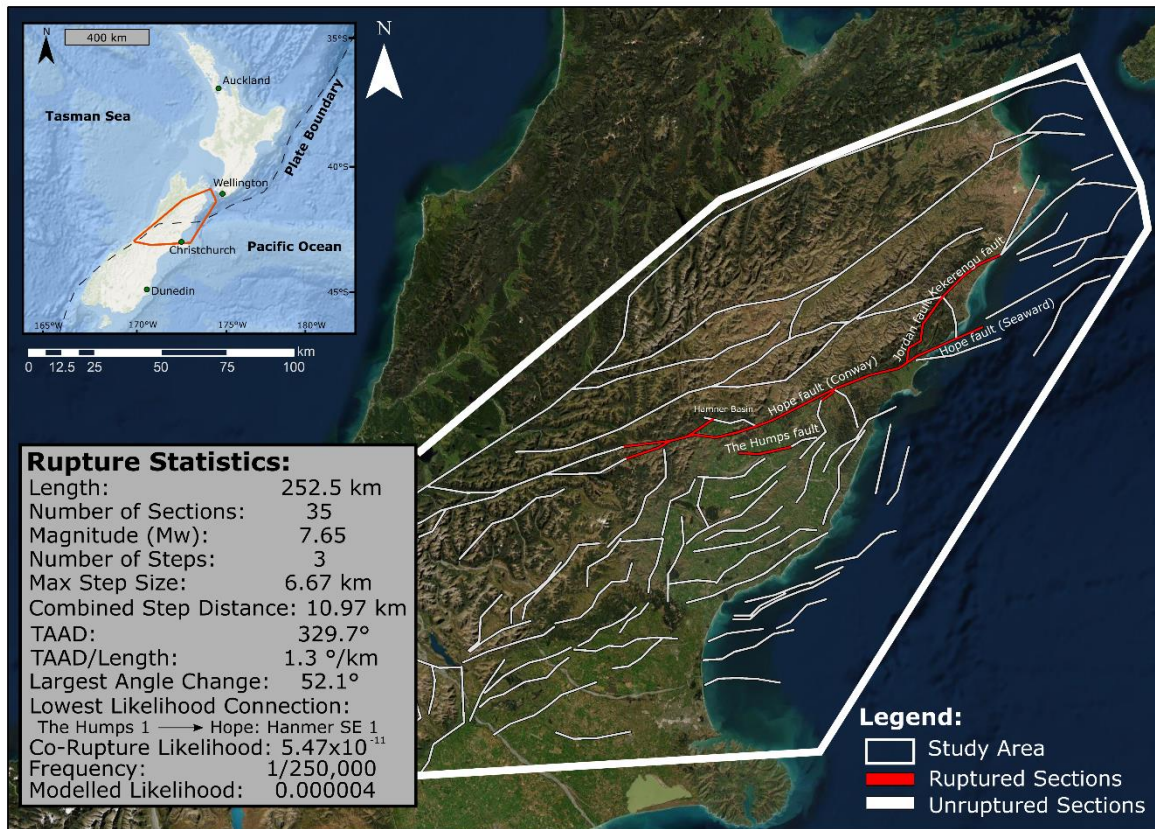


Figure 10: A Kaikoura-type earthquake involving rupture of The Humps and Kekerengu faults, the latter of which accounted for the majority of seismic moment release in the earthquake (Hamling et al., 2017; Litchfield et al., 2018). Note that the Kaikoura earthquake did not rupture the Hope fault, though all of our Kaikoura-type events required rupture. Other complex earthquakes including North Canterbury faults (i.e. those south of the Hope fault) also rarely took place.

Conclusions

We created a numerical, semi-empirical rupture simulator based on the surface rupture databases of Wesnousky (2008, Biasi et al. (2013), and Biasi and Wesnousky (2016, 2017). Our preferred model computes a passing probability for each fault connection in a modified version of the New Zealand Community Fault Model based on five geometric and kinematic variables. The preferred model rupture set conform to measures of overall rupture complexity in historical earthquakes, to paleoseismic estimates of moment magnitude, and with structural segmentation properties of long faults. When applied to the epicentral fault section of the 2016 Kaikoura earthquake, the majority of ruptures arrest at the fault tips or adjacent sections of other faults, but a few (<1%) result in higher magnitude, complex 'Kaikoura-type' events.. The ERS could be a means to weight rupture scenarios in seismic hazard assessments or estimate maximum likely magnitudes for seed faults or regions. With further development the ERS could incorporate geological slip rates to make results directly comparable to other simulators.

Acknowledgements

This project was funded by an EQC Biennial Grant to Stahl. We'd like to thank Russ Van Dissen, Mark Stirling, Rob Langridge, Andy Nicol, and Matt Gerstenberger for preliminary discussions regarding the project. The QuakeCoRE Surface Rupture and Slope Stability group is kindly acknowledged for its support and fruitful discussions.

Supplementary Information

- More detail on kinematic change parameter
- More detail on model operation and algorithm
- Auxiliary results

FIGURES:

- (1) Fuzzy logic schematic
- (2) Maximum length event for each model run
- (3) Curvature vs. length density maps

References

- Baker, J., B. Bradley, and P. Stafford (2021). *Seismic Hazard and Risk Analysis*, Cambridge University Press, Cambridge.
- Biasi G. P. Parsons T. Weldon R. J. Dawson T. E. (2013). Appendix J: Fault-to-fault rupture probabilities, U.S. Geol. Surv. Open-File Rept. 2013-1165-J , and California Geol. Surv. Special Rept. 228-J.
- Biasi, G. P., and S. G. Wesnousky (2016). Steps and Gaps in Ground Ruptures: Empirical Bounds on Rupture Propagation, *Bull. Seismol. Soc. Am.* **106** 1110-1124.
- Biasi, G. P., and S. G. Wesnousky (2017). Bends and Ends of Surface Ruptures, *Bull. Seismol. Soc. Am.* **107** 2543-2560.
- Biasi, G.P., and S.G. Wesnousky (2021). Rupture Passing Probabilities at Fault Bends and Steps, with Application to Rupture Length Probabilities for Earthquake Early Warning, *Bull. Seismol. Soc. Am.* **111** 2235-2247.
- Chamberlain, C. J., W. B. Frank, F. Lanza, J. Townend, and E. Warren-Smith (2021). Illuminating the Pre-, Co-, and Post-Seismic Phases of the 2016 M7.8 Kaikōura Earthquake With 10 Years of Seismicity, *Journal of Geophysical Research: Solid Earth* **126** e2021JB022304.
- Cowan, H. A. (1991). The North Canterbury earthquake of September 1, 1888, *Journal of the Royal Society of New Zealand* **21** 1-12.
- Cowan, H. A., and M. S. McGlone (1991). Late Holocene displacements and characteristic earthquakes on the Hope River segment of the Hope Fault, New Zealand, *Journal of the Royal Society of New Zealand* **21** 373-384.
- Field, E. H., R. J. Arrowsmith, G. P. Biasi, P. Bird, T. E. Dawson, K. R. Felzer, D. D. Jackson, K. M. Johnson, T. H. Jordan, C. Madden, A. J. Michael, K. R. Milner, M. T. Page, T. Parsons, P. M. Powers, B. E. Shaw, W. R. Thatcher, R. J. Weldon, II, and Y. Zeng (2014). Uniform California Earthquake Rupture Forecast, Version 3 (UCERF3)—The Time-Independent Model, *Bull. Seismol. Soc. Am.* **104** 1122-1180.
- Field, E. H., T. H. Jordan, M. T. Page, K. R. Milner, B. E. Shaw, T. E. Dawson, G. P. Biasi, T. Parsons, J. L. Hardebeck, A. J. Michael, R. J. Weldon, II, P. M. Powers, K. M. Johnson, Y. Zeng, K. R. Felzer, N. v. d. Elst, C. Madden, R. Arrowsmith, M. J. Werner, and W. R. Thatcher (2017). A Synoptic View of the Third Uniform California Earthquake Rupture Forecast (UCERF3), *Seismol. Res. Lett.* **88** 1259-1267.
- Hamling, I. J., S. Hreinsdóttir, K. Clark, J. Elliott, C. Liang, E. Fielding, N. Litchfield, P. Villamor, L. Wallace, T. J. Wright, E. D’Anastasio, S. Bannister, D. Burbidge, P. Denys, P. Gentle, J. Howarth, C. Mueller, N. Palmer, C. Pearson, W. Power, P. Barnes, D. J. A. Barrell, R. Van Dissen, R. Langridge, T. Little, A. Nicol, J. Pettinga, J. Rowland, and M. Stirling (2017). Complex multifault rupture during the 2016 M_w 7.8 Kaikōura earthquake, New Zealand, *Science*.
- Harris, R. A., and S. M. Day (1993). Dynamics of fault interaction: parallel strike-slip faults, *Journal of Geophysical Research: Solid Earth* **98** 4461-4472.
- Khajavi, N., R. M. Langridge, M. C. Quigley, C. Smart, A. Rezanejad, and F. Martín-González (2016). Late Holocene rupture behavior and earthquake chronology on the Hope fault, New Zealand, *GSA Bulletin* **128** 1736-1761.
- Langridge, R. M., and K. R. Berryman (2005). Morphology and slip rate of the Hurunui section of the Hope Fault, South Island, New Zealand, *New Zeal. J. Geol. Geophys.* **48** 43-57.
- Langridge, R. M., P. C. Almond, and R. P. Duncan (2013). Timing of late Holocene paleoearthquakes on the Hurunui segment of the Hope fault: Implications for plate boundary strain release through South Island, New Zealand, *GSA Bulletin* **125** 756-775.
- Li, Z., and B. Zhou (2018). Influence of fault steps on rupture termination of strike-slip earthquake faults, *J. Seismol.* **22** 487-498.
- Litchfield, N. J., P. Villamor, R. J. V. Dissen, A. Nicol, P. M. Barnes, D. J. A. Barrell, J. R. Pettinga, R. M. Langridge, T. A. Little, J. J. Mountjoy, W. F. Ries, J. Rowland, C. Fenton, M. W. Stirling, J. Kearse, K. R. Berryman, U. A. Cochran, K. J. Clark, M. Hemphill-Haley, N. Khajavi, K. E. Jones,

- G. Archibald, P. Upton, C. Asher, A. Benson, S. C. Cox, C. Gasston, D. Hale, B. Hall, A. E. Hatem, D. W. Heron, J. Howarth, T. J. Kane, G. Lamarche, S. Lawson, B. Lukovic, S. T. McColl, C. Madugo, J. Manousakis, D. Noble, K. Pedley, K. Sauer, T. Stahl, D. T. Strong, D. B. Townsend, V. Toy, J. Williams, S. Woelz, and R. Zinke (2018). Surface Rupture of Multiple Crustal Faults in the 2016 Mw 7.8 Kaikōura, New Zealand, Earthquake, Bull. Seismol. Soc. Am. **108** 1496-1520.
- Milner K. R. Page M. T. Field E. H. Parsons T. Biasi G. P. Shaw B. E. (2013c). Appendix T: Defining the inversion rupture set via plausibility filters, U.S. Geol. Surv. Open-File Rept. 2013-1165-T , and California Geol. Surv. Special Rept. 228-T.
- Nicol, A., J. Begg, V. Saltogianni, V. Mouslopoulou, O. Oncken, and A. Howell (2022). Uplift and fault slip during the 2016 Kaikōura Earthquake and Late Quaternary, Kaikōura Peninsula, New Zealand, New Zeal. J. Geol. Geophys. 1-16.
- Nicol, A., N. Khajavi, J. R. Pettinga, C. Fenton, T. Stahl, S. Bannister, K. Pedley, N. Hyland-Brook, T. Bushell, I. Hamling, J. Ristau, D. Noble, and S. T. McColl (2018). Preliminary Geometry, Displacement, and Kinematics of Fault Ruptures in the Epicentral Region of the 2016 Mw 7.8 Kaikōura, New Zealand, Earthquake, Bull. Seismol. Soc. Am. **108** 1521-1539.
- Oglesby, D. (2008). Rupture Termination and Jump on Parallel Offset Faults, Bull. Seismol. Soc. Am. **98** 440-447.
- Parsons, T., E. H. Field, M. T. Page, and K. Milner (2012). Possible Earthquake Rupture Connections on Mapped California Faults Ranked by Calculated Coulomb Linking Stresses, Bull. Seismol. Soc. Am. **102** 2667-2676.
- Robinson, R. (2004). Potential earthquake triggering in a complex fault network: the northern South Island, New Zealand, Geophys. J. Int. **159** 734-748.
- Seebeck H, Van Dissen R, Litchfield N, Barnes P, Nicol A, Langridge R, Barrell DJA, Villamor P, Ellis S, Rattenbury M, Bannister S, Gerstenberger M, Ghisetti F, Sutherland R, Fraser J, Nodder S, Stirling M, Humphrey J, Bland K, Howell A, Mountjoy J, Moon V, Stahl T, Spinardi F, Townsend D, Clark K, Hamling I, Cox S, de Lange W, Wopereis P, Johnston M, Morgenstern R, Coffey G, Eccles JD, Little T, Fry B, Griffin J, Townend J, Mortimer N, Alcaraz S, Massiot C, Rowland J, Muirhead J, Upton P, Hirschberg H, Lee J, 2022, New Zealand Community Fault Model – version 1.0. Lower Hutt (NZ): GNS Science. 96 p. (GNS Science report; 2021/57). doi: 10.21420/GA7S-BS61
- Shaw, B. E., K. R. Milner, E. H. Field, K. Richards-Dinger, J. J. Gilchrist, J. H. Dieterich, and T. H. Jordan (2018). A physics-based earthquake simulator replicates seismic hazard statistics across California, Science Advances **4** eaau0688.
- Shaw, B. E., B. Fry, A. Nicol, A. Howell, and M. Gerstenberger (2022). An Earthquake Simulator for New Zealand, Bull. Seismol. Soc. Am. **112** 763-778.
- Stirling, M., G. McVerry, M. Gerstenberger, N. Litchfield, R. Van Dissen, K. Berryman, P. Barnes, L. Wallace, P. Villamor, R. Langridge, G. Lamarche, S. Nodder, M. Reyners, B. Bradley, D. Rhoades, W. Smith, A. Nicol, J. Pettinga, K. Clark, and K. Jacobs (2012). National Seismic Hazard Model for New Zealand: 2010 Update, Bull. Seismol. Soc. Am. **102** 1514-1542.
- Van Dissen R, Seebeck H, Litchfield N, Barnes P, Nicol A, Langridge R, Barrell DJA, Villamor P, Ellis S, Rattenbury M, et al. 2021. Development of the New Zealand Community Fault Model – version 1.0. In Proceedings of the New Zealand Society for Earthquake Engineering Annual Conference 2021; Christchurch, New Zealand.
- Wesnousky, S. G. (2006). Predicting the endpoints of earthquake ruptures, Nature **444** 358-360.
- Wesnousky, S. G. (2008). Displacement and Geometrical Characteristics of Earthquake Surface Ruptures: Issues and Implications for Seismic-Hazard Analysis and the Process of Earthquake Rupture, Bull. Seismol. Soc. Am. **98** 1609-1632.
- Wesnousky, S. G., and G. P. Biasi (2011). The Length to Which an Earthquake Will Go to Rupture, Bull. Seismol. Soc. Am. **101** 1948-1950.

Zinke, R., J. Hollingsworth, J. F. Dolan, and R. Van Dissen (2019). Three-Dimensional Surface Deformation in the 2016 MW 7.8 Kaikōura, New Zealand, Earthquake From Optical Image Correlation: Implications for Strain Localization and Long-Term Evolution of the Pacific-Australian Plate Boundary, *Geochem. Geophys. Geosyst.* **20** 1609-1628.